EDGE ARTICLE

Wavelength dependent photochemistry of an iron dinitrogen hydride complex *via* multiple spectroscopies – competing ejection of axial ligands†

Weibing Dong, [ID] ‡[a] Hongxin Wang, [ID] ‡*[b] Saeed Kamali,[c] David R. Tyler, [ID] [d] Yisong Guo, [ID] [e] Lifen Yan,[f] Chantal G. Balesdent,[d] Justin L. Crossland,[d] David A. Case,[g] Yoshitaka Yoda,[h] Jiyong Zhao[f] and Stephen P. Cramer*[b]

Nitrogenase (N$_2$ase) is a critical enzyme which catalyzes the reaction of N$_2$ → NH$_3$ in nature. Studies on the spectroscopy and photochemistry of *trans*-[Fe^{II}(DMeOPrPE)$_2$(N$_2$)H][BPh$_4$] (**1**) and its isotopologues (**2–6**) provide a possible first step to evaluate the geometries and properties of the real N$_2$ase–N$_2$ structure(s). In this article, we have used FT-IR, FT-Raman, synchrotron-based nuclear resonant vibrational spectroscopy (NRVS) and DFT calculations to examine and assign the normal modes of these complexes. In addition, we have monitored their wavelength dependent photochemistry using mid-IR, near-IR, NRVS, and Mössbauer spectroscopies. Two distinct photolysis pathways are observed with mid-IR at (nominal) 4 K – (1) the cleavage of Fe–N$_2$ bond in UV or visible light photolyses, which presents a unipolar disappearance of the N$_2$ peak at 2094 cm^{-1} and is recombinable; (2) the ejection of *trans* hydrogen atom with UV irradiation, which has a pair of bipolar peaks with the disappearance of N$_2$ at 2094 cm^{-1} and the appearance of a new species at 2056 cm^{-1} and is non-recombinable. The latter peak is well aligned with the N$_2$ peak in an Fe^I reference complex (**7**). The combination of mid IR monitored photolysis/recombination and NRVS monitored photolysis form the central evidence for the conclusions in this article. In particular, the Fe^{II}–N$_2$ and Fe^I–H·dissociations are in competition with each other in UV or UV-inclusive photolyses of this dinitrogen hydride complex. In addition, near-IR and Mössbauer also provide consistent evidence about Fe^I. This wavelength dependent photochemical work is the first one on a reaction active N$_2$ase–N$_2$ model complex and it also demonstrates the competition ejection between two axial ligands (H· and N$_2$). It offers valuable information for future studies on real N$_2$ase–N$_2$ and its photolysis products.

Introduction

Nitrogenase (N$_2$ase) is a critical enzyme in nature that catalyzes the reduction of the atmosphere dinitrogen (N$_2$) to soil-usable

[a]*School of Life Science, Liaoning Normal University, Dalian 116081, China*

[b]*SETI Institute, 339 Bernardo Ave, Mountain View, CA 94043, USA. E-mail: hongxin. ucd@gmail.com; spjcramer@mac.com*

[c]*Department of Physics and Astronomy, Middle Tennessee State University, Murfreesboro, TN 37132, USA*

[d]*Department of Chemistry and Biochemistry, University of Oregon, Eugene, OR 97403, USA*

[e]*Department of Chemistry, Carnegie Mellon University, Pittsburgh, PA 15213, USA*

[f]*Advanced Photon Source, Argonne National Laboratory, Argonne, IL 60439, USA*

[g]*Department of Chemistry & Chemical Biology, Rutgers University, Piscataway, NJ 08854, USA*

[h]*Precision Spectroscopy Division, SPring-8/JASRI, Sayo-cho, Sayo-gun, Hyogo 679-5198, Japan*

† Electronic supplementary information (ESI) available: Experimental details and additional figures. See DOI: https://doi.org/10.1039/d5sc03870g

‡ These authors contribute equally.

ammonia (NH$_3$).[1–3] This nitrogen fixation process is required for all forms of life. MoFe N$_2$ases are the best-studied versions of N$_2$ase, and X-ray crystallography has provided a 1 Å resolution structure for the resting state 'FeMo cofactor' at the active site.[4] Kinetic studies indicate that N$_2$ can bind to this cluster (the active site) at the EPR-silent 3-electron reduced level E$_3$,[5] while EPR and ENDOR data show that N$_2$ also binds at the EPR-active E$_4$ level.[5–7] Fig. 1a illustrates the enzyme's catalytic circle with the proposed N$_2$ bonding states (E3 and E4). Fig. 1b shows a possible structure of FeMo cofactor bound to N$_2$, while b′ shows three different N$_2$ and H bonding models to FeMo cofactor cage. A better understanding of the initial interaction of N$_2$ with the active site is obviously critical to understanding the N$_2$ase mechanism (Fig. 1a). But to date, there is no vibrational data that might assist with the determination of the N$_2$ase–N$_2$ binding geometries or the strength of backbonding for the earliest stages of N$_2$ reduction.

As a step towards vibrational spectroscopy of N$_2$ase–N$_2$, we have investigated the spectroscopy and photochemistry of an
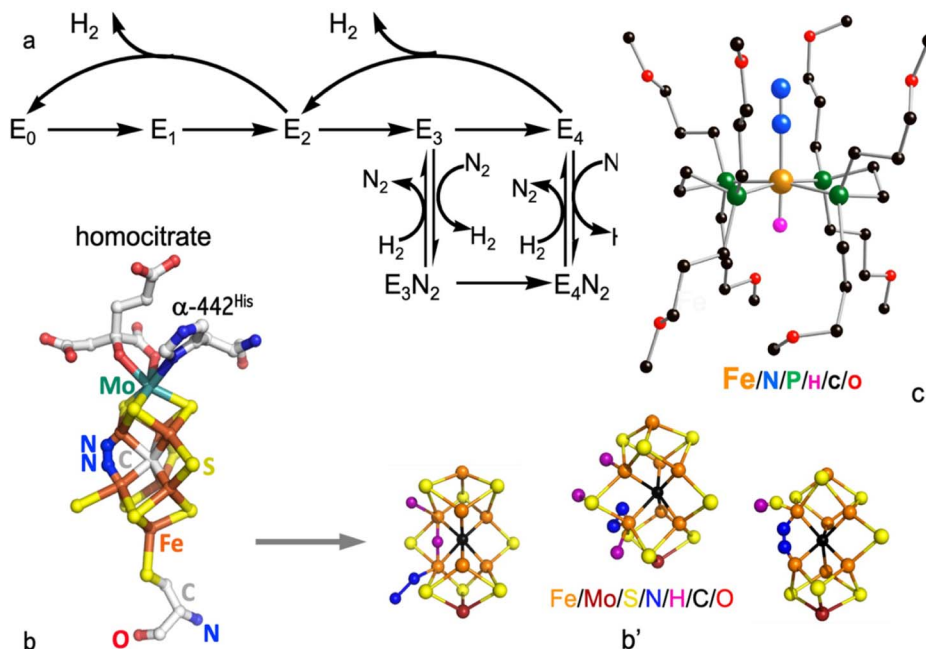
Fig. 1 (a) Proposed N_2 binding states in N_2ase enzyme's catalytic reactions; (b) a possible structure of the FeMo cofactor bound to N_2; (b') FeMo cofactor bound to N_2 with three different bonding models; (c) crystal structure of the complex **1**. The atoms in (b') and (c) are indicated with the color text under each figure.

N_2-bound Fe model complex: *trans*-[Fe(DMeOPrPE)$_2$(N_2)H]$^+$ (DMeOPrPE = 1,2-bis(bis(methoxypropyl)phosphino)-ethane), **1**, and its isotopologues: [Fe(DMeOPrPE)$_2$(N_2)D]$^+$, **2**, [Fe(DMeOPrPE)$_2$($^{15}N_2$)H]$^+$, **3**, [^{57}Fe(DMeOPrPE)$_2$(N_2)H]$^+$, **4**, [^{57}Fe(DMeOPrPE)$_2$(N_2)D]$^+$, **5**, and [^{57}Fe(DMeOPrPE)$_2$($^{15}N_2$)H]$^+$, **6**. This complex contains a low-spin Fe^{II} with a very weakly activated N_2 (as indicated by the N–N stretching frequency ν(N≡N) = 2094 cm^{-1}).[8–12] There is an additional axial ligand H in the *trans* position with N_2, as shown in Fig. 1c, mimicking the N_2 and H bonding at FeMo cofactor to some extent. Other ligands (P/C/O *etc.*) are irrelevant to the photochemical discussions in this study. Chemical removal of the proton (H$^+$) produces a formal Fe^0 complex [with ν(N≡N) = 1966 cm^{-1}] and NH$_4^+$ with a 15% yield upon reaction with triflic acid, showing $N_2 \rightarrow NH_3$ reaction activities.[9] In this paper we report results from a combination of FT-IR, FT-Raman, synchrotron radiation based ^{57}Fe nuclear resonance vibrational spectroscopy (NRVS),[13–16] and DFT calculations[16] to investigate the vibrational properties of this complex and its isotopologues. In addition, we have monitored the UV-visible light induced photochemical dynamics using a combination of FT-IR, NRVS and Mössbauer spectroscopies. The competition between two dissociation reactions involving net loss of either N_2 or H axial ligand(s) has been revealed. To model the photolysis product, [Fe^I(DMeOPrPE)$_2$(N_2)]$^+$,[17] **7** (or **1** without H and with an Fe^I instead of an Fe^{II}), was also studied *via* IR and DFT calculation. Our motivation stems from photolysis studies of CO-inhibited N_2ase, which have yielded a plethora of signals from photochemical difference FT-IR spectra,[18,19] and the hope to use IR and other spectroscopic methods to evaluate N_2ase–N_2 in the future.

Since this complex serves as a structural model for one possible type of N_2ase–N_2 binding geometry, the observed photochemistry serves as a useful guide for future experiments on the real N_2ase–N_2 enzyme.

Results and discussion

Higher frequency vibrational spectroscopy

Vibrational spectra for **1**, in the range from 1200 to 2200 cm^{-1}, are illustrated in Fig. 2. Along with miscellaneous ligands and counterion bands, this region contains the more photochemically interesting Fe–H and N≡N stretching modes. Curves in Fig. 2a are from FT-Raman measurements while the ones in Fig. 2b are from FT-IR. In the IR spectrum, the strongest band comes from the N≡N stretch, which is seen at 2087 cm^{-1} for **1** (measured in sealed sample/KBr pellets at room temperature), and at 2017 cm^{-1} for the $^{15}N_2$ isotopologue, **3**. The N≡N stretching bands are also strong in the FT-Raman spectra (Fig. 2a, measured in powders at 77 K). DFT calculations gave the N≡N stretching frequency as 2108 cm^{-1} for $^{14}N_2$ and 2038 cm^{-1} for $^{15}N_2$, as shown in Table 1 and Fig. S1 in the ESI.† Although the absolute positions are different, the natural abundance → $^{15}N_2$ shifts are −70 cm^{-1} for both observed and DFT calculated spectra (Fig. S1†).

The Fe–H/D stretching modes are much harder to observe. There is scant evidence for such bands in the IR, but a candidate Fe–H band can be seen at 1928 cm^{-1} in the FT-Raman. The Fe–H assignment in FT-Raman is confirmed by the band shift to 1381 cm^{-1} in the spectrum of the D isotopologue, **2** (Fig. 2a): 1928/1381 ∼ 1.4. The DFT calculations predict a weak IR signal for the Fe–H stretch at 1924 cm^{-1} (Fig. S1†), but the calculated
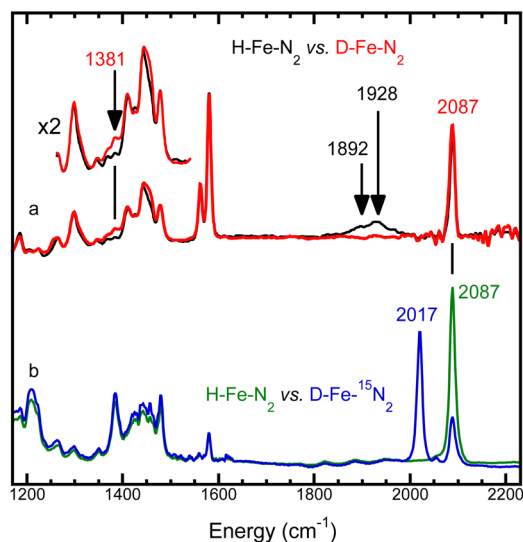
Fig. 2 Vibrational spectra in the higher frequency region for **1** and its isotopologues. (a) FT-Raman of **1** (black) vs. D-substituted version (**2**) (red) measured at 77 K; (b) FT-IR for **1** (green) vs. $^{15}N_2$-substituted version (**3**) (blue) measured in sealed KBr pellets at room temperature. Peak features without labels are from 'irrelevant' ligand or counterion modes.

Raman spectrum provides clear evidence for Fe–H stretch at 1924 cm^{-1} for **1**, which shifts to 1372 cm^{-1} for **2** (Fig. S2†): 1924/1372 ~ 1.4. This is in good accordance with the experimental observation in Fig. 2.

There is also marginal evidence for a second Fe–H related feature at about 1892 cm^{-1}, but there is only one Fe–H peak in the DFT calculation (Fig. S2†). A sharp Fe–H peak in DFT vs. multiple weak peaks in the observed spectrum is not rare due to miner side products or isomers or different symmetries etc., such as the ones in a previous NRVS publication.[20]

The proposed Fe–H stretching frequencies are slightly lower than the Fe–H stretch seen at 1960 cm^{-1} in [FeH(dppe)$_2$]BPh$_4$

but compare favorably with the Fe–H stretches seen at 1902 and 1868 cm^{-1} in green and yellow forms of [FeH(N$_2$)(dppe)$_2$]BPh$_4$.[21] NRVS also shows a "stand alone" Fe–H peak at 1915 cm^{-1} due to a combined contribution from HFe(H$_2$) and HFe(N$_2$) entities in another iron hydride complex.[22] This peak is again in the region near 1928 or 1892 cm^{-1} observed for our complex **1**.

Lower frequency vibrational spectroscopy

The vibrational spectra for **1** and its isotopologues in the lower frequency region from 400 to 900 cm^{-1} are shown in Fig. 3, while the ones in the whole energy region at 0–950 cm^{-1} are in Fig. S3.†

Again, the most photochemically interesting features are those related to the N$_2$ and H ligands. There is little evidence for Fe–N$_2$ stretching and bending features in the FT-Raman spectra (Fig. 3a), but IR bands in the 440–470 cm^{-1} region are good candidates for such modes (Fig. 3b). The assignment is clarified by the NRVS (Fig. 3c), which only senses modes with Fe in motion.[13–16] The strongest ^{57}Fe NRVS band for natural abundance N and H (**4**) is at 466 cm^{-1}, and this band downshifts to 457 cm^{-1} with $^{15}N_2$ substitution (**6**), allowing unambiguous identification of it as a band related to Fe–N$_2$ motion. The DFT calculated NRVS yields Fe–N$_2$ modes at modestly higher frequencies, but the 7 cm^{-1} downshift from 494 cm^{-1} to 487 cm^{-1} with $^{15}N_2$ substitution (Fig. 3d) agrees well with the 9 cm^{-1} experimental downshift (Fig. 3c blue vs. red). By comparison, the Fe–N$_2$ stretch and bend modes for a similar complex [FeH(N$_2$)(depe)$_2$]BPh$_4$ were assigned respectively at 479 and 487 cm^{-1},[24] and with $^{15}N_2$ substitution, these modes downshifted by 7 and 5 cm^{-1} respectively. The spectral difference between our **1** (or **3**) and the reported [FeH(N$_2$)(depe)$_2$]BPh$_4$ could be due to different ligands the two complexes have and different measurement conditions, such as energy resolutions, sample states, and temperatures. It seems reasonable to conclude that the Fe–N$_2$ stretch and bend modes are unresolved in our NRVS (c) or far IR (b) data and the NRVS vs. IR peaks around 366 cm^{-1} are almost overlapped with each other (Fig. 3c

Table 1 Summary of observed and DFT-calculated vibrational peak positions

	N≡N stretch [cm^{-1}]	Fe–H/D stretch [cm^{-1}]	Fe–H/D bend [cm^{-1}]	Fe–N$_2$ bend/stretch [cm^{-1}]
HFe^{14}N$_2$	2087[a,b]	1892[b]	1892[b]	460[a]
		1928[b]	1928[b]	466[c]
	2018[e]	1924[e]	807[f]	494[d]
	2108[d]		752[f]	494[f]
			739[f]	
HFe^{15}N$_2$	2017[a,b]			454[a]
				457[c]
	2038[e]			487[d]
	2038[d]			487[f]
DFe^{14}N$_2$	2087[a,b]	1381[b]	593[c]	463[c]
			610[c]	
	2105[e]	1372[e]	595[f]	493[d]
	2105[d]		614[f]	494[f]

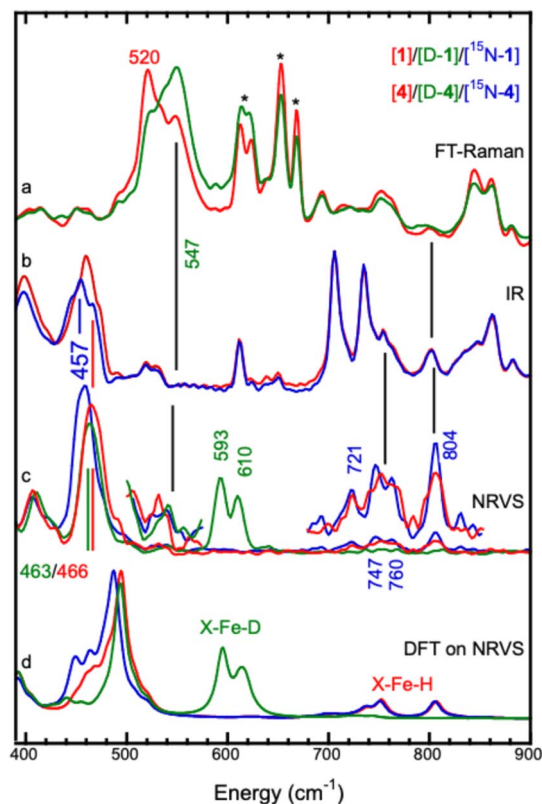[a] FT-IR. [b] FT-Raman. [c] NRVS. [d] DFT on IR. [e] DFT on Raman. [f] DFT on NRVS.

Fig. 3 Vibrational spectra in the lower frequency region for **1** and isotopologues: (a) FT-Raman for **1** (red) and (**2**) (green) measured at 77 K; (b) FT-IR for **1** (red) and **3** (blue) measured at room temperature; (c) NRVS for **4** (red), **5** (green) and **6** (blue) measured at 10 K (nominal temperature, or 40–60 K – the real sample temperature[23]); and (d) DFT calculation of NRVS for **4** (red), **5** (green) and **6** (blue). The peaks with * are transitions related to 'irrelevant' ligands or counter ions.

vs. 3b). This is consistent with the general observation for a single ^{57}Fe centered complex.[14,25,26] Nevertheless, the profile around 466 cm^{-1} in Fig. 3c is the characteristic 'peak' to monitor the Fe–N$_2$ with NRVS.

As for Fe–H/D-related modes, there is a pair of reasonably strong NRVS bands at 593 and 610 cm^{-1} in the NRVS for **5** (the D isotopologue), which shift to a set of weak features at 721, 753 (a combined centroid for **1** or peaks at 747 and 760 for **3**), and 804 cm^{-1} in the NRVS for **4** (Fig. 3c). For comparison, we recently observed a mostly Fe–D bend at 613 cm^{-1} for the D isotopologue of a related complex, [(H/D)FeCO(dppe)$_2$]BF$_4$, shifting to a pair of small Fe–H peaks at 727 and 746 cm^{-1}.[27] Furthermore, for [Fe(H/D)(N$_2$)(depe)$_2$]BPh$_4$,[24] the Fe–H (Fe–D) bends were assigned to 783 cm^{-1} (596, 583, 574 cm^{-1}) respectively.[24] It seems reasonable to assign our NRVS features to the same types of vibrational modes. In addition, DFT calculation well reproduced the overall NRVS spectral profiles, as well as the isotopic shifts. The presence of multiple bands in the Fe–D and Fe–H bending regions can be explained by the symmetry of the bend modes and extensive coupling with the *trans* ligand.[27] Another strong feature, at 520 cm^{-1} in the FT-Raman for **1**, upshifts to 547 cm^{-1} with D substitution (**2**). With considerable expansion, similar features

can be seen as a very weak band in the NRVS. For the moment, we call this unassigned peak 'band X'.

Mid-IR-monitored photochemistry

Mid-IR (MIR) refers to the IR bands in the 400–4000 cm^{-1} region. MIR absorption (measured with FT-IR) is one of the most frequently used spectroscopic methods to study vibrational properties. Here, MIR monitored difference spectra before and after the photolysis of complex **1** at cryogenic temperature (maintained at 4 K) are illustrated in Fig. 4 (in the ~1800–2200 cm^{-1} region). The photolysis light and the IR light were introduced *via* different routes (perpendicular setup) and all the photolysis wavelengths >300 nm were available. Narrower wavelength selection can be made *via* using optical filters. The overall MIR difference spectra reveal at least two distinct photolysis patterns that depend on the wavelength of the photolysis radiation. Photolysis with visible light, for example using 502 ± 10 nm, shows a unipolar loss of the N≡N stretching band at 2094 cm^{-1}, indicating photo-detachment of the N$_2$ ligand from the sample(s) (Fig. 4a). The band shift to 2094 cm^{-1} from 2087 cm^{-1} (as shown in Fig. 2b → 4a) reflects both room temperature *vs.* 4 K and solid state *vs.* THF solution. For the moment, we will call this unipolar photolysis product 'species V'. In the same spectrum (Fig. 4a), there is a weak derivative-like feature with negative intensity in the 1850–1880 cm^{-1} region and a positive product at ~1900–1930 cm^{-1}. This region is assigned to the Fe–H stretching mode (in reference to Fig. 2a), and the shift to higher frequencies suggests that the photolysis product is more tightly bound, consistent with a stronger Fe–H bond upon dissociation of the *trans* N$_2$ ligand. When complex **1** was irradiated with a wavelength in the region of 372 ± 8 nm – 502 ± 10 nm (in Fig. 4a, b and S4† and other testing experiments without figures), the same photolysis pattern was observed – a unipolar loss of the v(N≡N) feature.

There is no photolysis effect observed at several wavelengths longer than 502 ± 10 nm, such as at 516 ± 10 nm, 540 ± 10 nm, and 579 ± 9 nm. In addition, no photolysis effect was observed from an alternative photolysis setup where the photolysis light was introduced *via* IR optical pathway. Then the wavelength <500 nm was effectively blocked by IR reflection mirrors in the FTIR instrument and ZnSe windows in the cryostat.

A different photolysis result was obtained from UV photolyses. For example, irradiation with a broad-band UV-inclusive beam from a Sutter Lambda LS light source leads to an obvious bipolar spectrum (Fig. 4c). The photolysis light output is similar with that shown in Fig. S5† and we call this condition UV photolysis case 1 (or UV1). In addition to the disappearance of the v(N≡N) band at 2094 cm^{-1} (we call its integrated intensity A, as illustrated in Fig. 4c'), there appears a positive feature at 2056 cm^{-1} (we call it B). However, this is not a balanced bipolar spectrum – it is obvious that A > B. Using a reflective IR mirror (a 'cold mirror') to reject IR related heat load from UV1 produces an even more unbalanced feature between A and B (Fig. 4d *vs.* c). UV2 includes the wavelength about 300–500 nm and we call it UV photolysis case 2 (or UV2). For a more quantitative evaluation, Fig. S6† summarizes the integrated
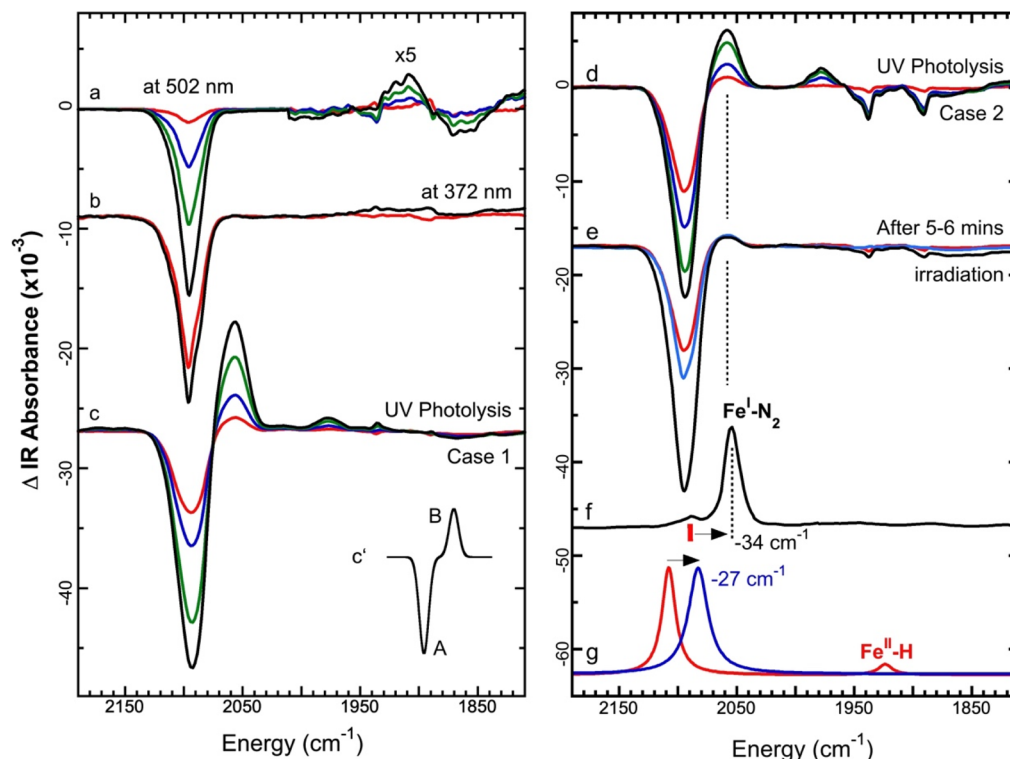
Fig. 4 MIR-monitored wavelength-dependent photolyses of **1** (measured in THF solution at 4 K): (a) photolysis at 502 ± 10 nm; (b) photolysis at 372 ± 8 nm; (c) UV-inclusive photolysis without optical filters (we call it UV photolysis case 1, or UV1); (4c') the illustration for a bipolar MIR spectrum (A vs. B); (d) UV-inclusive photolysis with an IR rejection mirror but without other filters (UV photolysis case 2, or UV2); (e) UV photolysis at 5–6 min with an IR rejection mirror (UV2, red), a 350 ± 30 nm bandpass filter (UV3, blue) and a 340 ± 13 nm bandpass filter (UV4, black); (f) the MIR spectrum of $[Fe^I(DMeOPrPE)_2(N_2)]^+$ (**7**) as an Fe^I model complex; (g) DFT calculations for IR spectra of **1** (red) vs. **7** (blue).

intensities at peak A and peak B vs. photolysis time for 0–55 min in a UV1 photolysis (MIR spectra exampled in Fig. 4c) and for 0–61 min in a UV2 photolysis (MIR spectra exampled in Fig. 4d). The intensities in B for both UV cases can be overlapped with each other when one of them is re-scaled to match the other, as shown in Fig. S6† (round symbols, red vs. blue) or Fig. 5 (round symbols, red vs. blue) – the A can be normalized in the same way, producing relative A as shown in Fig. 5. The comparison among these time course curves finds: (1) the signal size of A is larger than that of B in either UV1 or UV2. This suggests A and B do not represent the same process and at least two processes exist in UV photolyses; (2) the intensities in B for both UV cases can follow the same trend, leading to Fig. 5 (round symbols, red vs. blue). This suggests that the peak B for different photolysis cases can represent one type of process; (3) A does not follow the same trend in different UV photolyses no matter how the two curves are normalized, as shown in Fig. S6† (the red squares vs. the purple squares); (4) the relative signal size of A when normalized to the corresponding B (square symbols, red vs. blue in Fig. 5) are very different for UV1 and for UV2. Results (3) and (4) show that intensity A is photolysis source dependent while the only experimental difference between UV1 and UV2 is that UV2 used a cold mirror to reject the infrared radiation (the heat load) in its photolysis source. It seems reasonable to link the higher heat load in UV1 to its smaller 'relative A signal' (relative to the same B size). The mechanism could be linked to recombination process which will be discussed later.
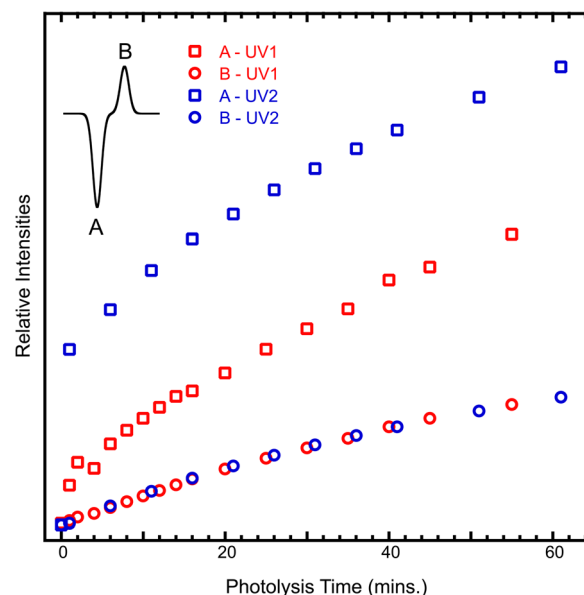

Fig. 5 The relative integrated intensities for peak A (square symbols) and for peak B (round symbols) as functions of photolysis time (mins.) for the UV photolysis case 1 (red) vs. case 2 (blue) when normalized to their original B sizes. The data is from MIR monitored UV photolyses of **1** (as those in Fig. 4c and d).

In addition, bandpass filters can also be used to select even narrower UV bands for photolysis (e.g. 350 ± 30 nm for UV3 or 340 ± 13 nm for UV4). The MIR spectra for UV2, UV3, UV4 at about 5–6 min irradiation time are compared in Fig. 4e, showing that B's intensities do not have significant variation among different UV photolysis cases while A's intensity for 340 ± 13 nm photolysis (UV 4) has an obviously larger size vs. UV3 and UV2 (probably due to different heat load).

In mathematics, the unbalanced A vs. B feature can be treated as the sum of a pure unipolar feature A′ (we call it 'species V') plus a balanced bipolar feature where A″ = B (we call it 'species U'). Then, branch B in Fig. 4c–e, or in Fig. 5 represents the signal for species U while A in these figures represents V + U (not just V or just U). This is consistent with the discussions in Fig. 5 which suggests that B represents one process while A could represent more than one process. With this approach, visible light photolysis leads to species V only (a pure unipolar feature) while UV photolysis produces species V + species U (not just species U). A hypothesis that assumes the H· detachment in UV photolyses could explain the balanced portion of a bipolar feature in the $\nu(N{\equiv}N)$ region (species U). Here, the interested readers can jump to Fig. 8 in the Summary and mechanisms section for better understanding the photolysis states mentioned but the overall photolysis hypothesis still need more results to summarize. We also use N_2-dissociated species to describe V and H·-dissociated species to describe U in most of the following text.

The downshift of 2094 → 2056 cm^{-1} (=−38 cm^{-1}) in Fig. 4c–e suggests that the N≡N bond becomes weaker (rather than stronger) after the photo-detachment of H·. This makes Fe^{II} → Fe^{I} be a possible reason. The $[Fe^{I}(DMeOPrPE)_2(N_2)]^+$ (7, Fig. 4f) is an Fe^{I} complex used to model the UV photolysis product of 1. Its MIR shows a $\nu(N{\equiv}N)$ peak at a lower energy position of 2053 cm^{-1}, a −34 cm^{-1} (=2053−2087) downshift from the that for 1 (an Fe^{II} complex) measured under the same condition. In Fig. 4f, MIR for 1 is not re-illustrated to save space but its Fe^{II}–N_2 position (2087 cm^{-1}, Fig. 2b) is indicated here with a red bar. The photolysis samples (Fig. 4a → e) were measured in THF solution at 4 K while the ref. 1 (Fig. 2b) and 7 (Fig. 4f) were measured in sealed KBr pellets at room temperature. Different measurement conditions could lead to different peak positions as well as peak position differences. DFT calculation was also performed on MIR spectra and presented in Fig. 4g: red for 1 and blue for 7. It shows a just little bit smaller downshift of −27 cm^{-1} in comparison with the observed downshift (Fig. 4c–e, 38 cm^{-1}). These results suggest the H·-dissociated species (U) can have an Fe^{I}. This is also consistent with the fact that the Fe^{0} complex via chemical removal of H^+ from complex 1 leads to a much lower $\nu(N{\equiv}N)$ at 1966 cm^{-1}.[9] DFT on 1 also has a clear Fe–H feature at 1924 cm^{-1} while 7 does not have, illustrating the absence of H in the latter. On the other hand, the N_2-dissociated species (V) is likely to keep a low spin Fe^{II} when N_2 is photo-dissociated because its Fe–N_2 peak position has almost no change.

In short, while visible light photolysis produces the dissociation of N_2 (species V), UV photolysis leads to the competitive dissociations of N_2 vs. H·, or in other word, the competitive

production of species V vs. species U. All the MIR monitored photolysis experiments find: (1) UV wavelength (e.g. <370 nm) must be included in order to produce a bipolar MIR signal and; (2) no A → B conversion was observed at all.

Mid-IR-monitored recombination

Photolysis products can recombine, e.g. the unipolar peak at 2094 cm^{-1} in the 502 nm photolysis for 1 can shrink after warming-up to appropriate temperatures. The recombination process can then be monitored via the relative IR intensity at 2094 cm^{-1} vs. the warming-up time at each temperature, as shown in Fig. 6a. The 502 nm photolysis product starts to have a significant recombination rate at as low as 13 K (Fig. 6a, red), and slow recombination can even be observed at 8 K (Fig. 6a, black). A relatively low activation energy of 388 J mol^{-1} was derived from an Arrhenius plot (the temperature dependence of the recombination rate, Fig. 6b). This activation energy is much lower than the CO recombination rate with N_2ases:[18] 3.7 kJ mol^{-1} for CO recombination with the wild-type Azotobacter vinelandii (Av) N_2ase or 3.3 kJ mol^{-1} for CO recombination with the α-H195Q substituted Av N_2ase. This predicts an easier and faster Fe–N_2 recombination for the photolysis product of 1 (and its isotopologues) in comparison with N_2ase–CO.

In comparison with the fast recombination after the 502 nm photolysis (as well as after other visible light photolyses), a far more complicated recombination process was observed after UV photolysis (e.g. via UV 1, Fig. 6c). For example, the feature at 2094 cm^{-1} (A) diminished by 12% when the sample was
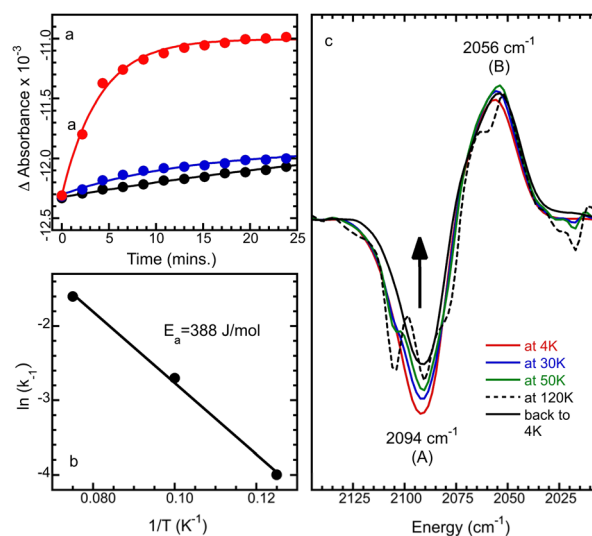

Fig. 6 MIR monitored recombination process: (a) the relative IR absorbance difference at 2094 cm^{-1} vs. the recombination times at 8.0 K (black), 10.2 K (blue), and 13.2 K (red) following the 502 nm photolysis at 4 K: observed data (filled symbols) vs. their exponential simulations (solid lines); (b) the Arrhenius plot of $\ln(k_{-1})$ vs. $1/T$, leading to a low activation energy of 388 J mol^{-1}; (c) IR difference spectra for 1 photolyzed with UV-inclusive light (UV case 1) prior to the recombination (red), being warmed up to 30 K (blue), 50 K (green), and 120 K (dashed back), and re-cooled from 120 K down to 4 K (solid black) respectively.

warmed up to 50 K (Fig. 6c, green vs. red) and 26% on average up to 120 K (dashed black vs. red) but the feature at 2056 cm^{-1} (B) has almost no change even at 120 K for 5 min. Some 'special features' (dashed black) were also observed at 120 K recombination whose nature is not clear at the moment. At least, these 'special features' disappear after we re-cooled 1 back down to 4 K (solid black). After this thermal cycle (back to 4 K), the signal at A (solid black) shrinks about 26% in comparison with the original photolysis product (red), but the change at B can be ignored. At this point, the signal ratio of A″/B″ is close to 1, the MIR signal becomes an almost 'balanced' bipolar signal. Therefore, we can conclude that N$_2$-dissociated species (V) is recombinable with N$_2$ with a pretty low activation energy while H·-dissociated species (U) is not recombinable with H· at all. The mechanism is not clear but the speculation could include H· being very reactive and being able to be captured by the environment (such as THF).

Based on the above discussions, the photodissociated N$_2$ species can in principle have in situ recombination in a high heat load photolysis process. This helps explain the smaller 'relative A intensities' in UV1 vs. those in UV2, UV3, UV4 in Fig. 4 and 5. These "abnormal" phenomena are due to the fact that a broad band photolysis can have a much larger recombination rate due to high heat load and thus a much less net photolysis rate (=photolysis rate – recombination rate) than a narrow band photolysis (e.g. UV4). Once again, no A → B conversion was found in all the evaluated recombination processes.

Preliminary NRVS monitored photochemistry

The NRVS can also be used to monitor photolysis on ^{57}Fe enriched 1, 2, 3 (which are 4, 5, 6). While MIR provides comprehensive information on ligand dissociation or recombination via monitoring the N≡N vibrational mode, NRVS can directly look at and focus on the Fe–H/D or Fe–N$_2$ bonds due to its ^{57}Fe specificity.[13–16] Sample 5 (instead of 4 or 6) was used in this study to monitor the photolysis process because the X–Fe–D bending signal for 5 is much stronger than the X–Fe–H for 4 or 6 (see Fig. 3c).

Our NRVS monitored photolysis is done with visible light irradiation at >370 nm (without UV). The light source has an output as shown in Fig. S6† but the light port at the NRVS cryostat is made of Lucite material which blocks UV shorter than 370 nm (or even longer). Indeed, although 5 was irradiated for more than 12 hours, there is no observable photolysis effect on the X–Fe–D feature within the range of the errorbar (Fig. 7a, red vs. blue) – meaning no H·-dissociated species (U) was found. This is consistent with the MIR observation that there is no Fe–H cleavage in the photolysis with wavelength >370 nm (Fig. 4a, b and S4†). In comparison with Fig. 3c, the Fe–D peak profile shifts from 593–610 cm^{-1} for the powder sample to 570–615 cm^{-1} for the THF solution (Fig. 7a).

In contrast, there is a noticeable intensity reduction in the Fe–N$_2$ profile (by $27 \pm 3\%$) centered at 463 cm^{-1}, suggesting Fe–N$_2$ dissociation (species V) indeed occurs under our NRVS photolysis condition. The smaller photolysis effect in NRVS spectra can be attributed to the in situ recombination of N$_2$-dissociated species (V) with N$_2$ because the real sample temperature is 80 K based on PHOENIX analysis.[13] NRVS sample is often extremely close to the room temperature window at its cryostat and its real sample temperature is often much higher than the sensor reading[23] (e.g. 10 K at the sensor).[13,23] The real sample temperature for non-photolysis sample was at 50 K and the photolysis light added more heat load. At 80 K, a large part of the photo-dissociated N$_2$ can be recombined, leaving
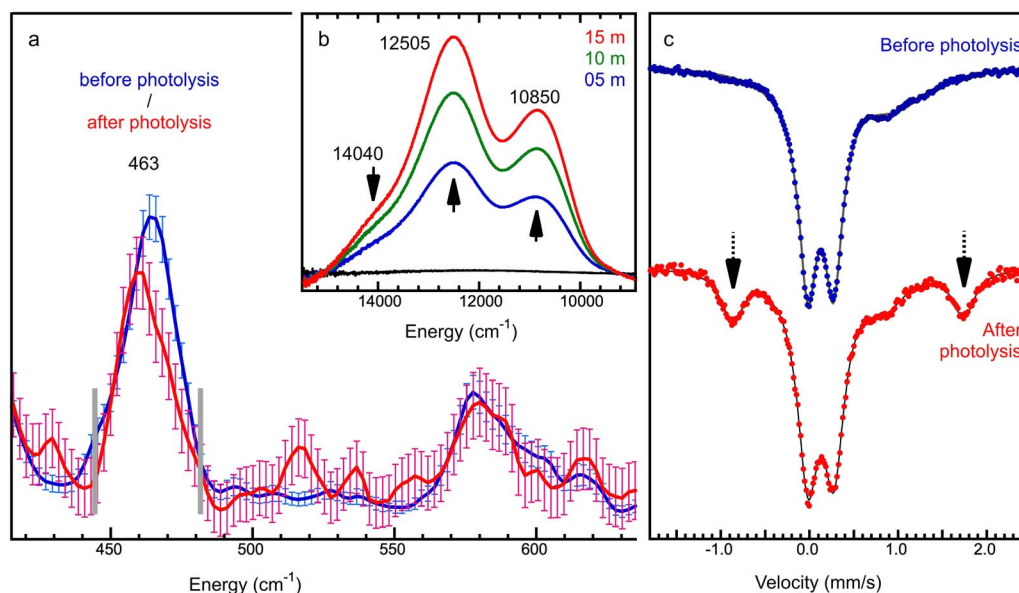

Fig. 7 (a) Visible light photolysis (wavelength >370 nm) of complex 5 (or 1-^{57}Fe/D) monitored with NRVS: blue = before the photolysis and red = in situ photolysis NRVS averaged from 1 hour to 13 hours with photolysis light on. The sample was maintained at 10 K (nominal) and was estimated to have a real temperature at 50 K for the non-photolysis sample and 80 K for the photolysis sample; (b) UV photolysis of 1 (via UV case 2) monitored by NIR difference spectra at 4 K for 5 (blue), 10 (green) 15 (red) mins.; (c) UV photolysis of 4 (via UV case 2) monitored with Mössbauer at 80 K: blue = Mössbauer spectrum before the photolysis and red = the one after the photolysis. The black thin lines are the fitted lines.

a smaller net dissociation signal (27%). The NRVS observation here again is consistent with the MIR results that significant *in situ* recombination can exist when the photolysis heat load is high (*e.g.* UV1).

The peak centroid also shifts to a bit lower energy position (-5 cm^{-1} for the peak position, -4 cm^{-1} for the centroid) as well, which could be due to the possible weaker Fe^{II}–N$_2$ bonding after recombination or due to the partial photo-reduction. This downshift is much smaller than the Fe^{II} → Fe^{I} shift (-38 cm^{-1}) observed in MIR and indeed the Fe–D (bending) peak does not change at all – meaning the minor shift is not likely to be attributed to the H· dissociation.

Other spectroscopy monitored photochemistry

Since part of the rationale for this study was to explore feasible route(s) to evaluate N$_2$ase–N$_2$ photochemistry in the future *via* multiple spectroscopies, we also monitored photolysis of **1** using other spectroscopic methods, such as near-IR (NIR) and Mössbauer spectroscopies for example. The results from them are summarized in Fig. 7b and c. While MIR and NRVS revealed the structural information about the bond dissociation(s)/ recombination, NIR and Mössbauer are excellent in providing electronic information, *e.g.* about the Fe's oxidation states. Following UV photolysis of **1** with UV2 at cryogenic temperature (4 K), the NIR difference spectrum shows two strong bands at 10 850 and 12 505 cm^{-1}, as well as a third weak peak at 14 040 cm^{-1} (Fig. 7b). These peaks occur in the typical region of d–d transition for a d^7 complex. For comparison, complex "[PhBPCH$_2$Cy$_3$]Fe^{I}" shows three peaks at 13 459, 9842 and 7168 cm^{-1} in visible and NIR regions.[28] The observation of the first NIR monitored UV photolysis on a metal–N$_2$-containing complex suggests that this might be a useful approach to evaluate N$_2$ase–N$_2$ samples in the future.

The Mössbauer monitored photolysis of **4** (^{57}Fe enriched **1**) is presented in Fig. 7c. Mössbauer experiment utilizes the similar photolysis radiation as UV2 at 80 K and should also produce both N$_2$-dissociated and H·-dissociated species (V + U). Before the photolysis, the Mössbauer spectrum consists of a major component centered at isomer shift $\delta_1 = 0.129$ mm s^{-1} with a quadrupole splitting $\Delta E_Q = 0.297$ mm s^{-1}. The values are typical for a low spin Fe^{II} species.[21,29] There is also evidence for minor other impurities in the sample. Upon photolysis, a completely new component appears at $\delta = 0.434$ mm s^{-1} and $\Delta E_Q = 2.611$ mm s^{-1}. This product has a higher centroid shift and much larger quadrupole splitting than a Fe^{II} and does not overlap with any components before the photolysis. In a Mössbauer correlation diagram,[29] this photolyzed species is identified as a low-spin Fe^{I} compound, which is consistent with the Mössbauer for a similar complex [Fe^{I}H(dppe)$_2$]BPh$_4$ reported ($\delta = 0.22$ mm s^{-1} and $\Delta E_Q = 1.527$ mm s^{-1}), and consist with our NIR and MIR results [about an Fe^{I}].

Summary and mechanisms

In this work, we have examined (a) the vibrational spectroscopy (FT-IR, FT-Raman, NRVS) of the terminally bound N$_2$ complex **1** or its isotopologues with D, ^{15}N$_2$, and/or ^{57}Fe substitution, (b) the photochemistry of **1** or its isotopologues monitored by multiple spectroscopies (MIR, NRVS, NIR and Mössbauer), and (c) the recombination of the photochemical products *via* MIR. The focus of this article is on MIR monitored photolysis/recombination as well as NRVS monitored photolysis, from which we found evidence for two types of photolysis products – (1) a species lacking the terminal N$_2$ ligand, most likely [Fe^{II}(DMeOPrPE)$_2$H]$^+$ (corresponding to N$_2$-dissociated species or V). This species has a unipolar disappearing peak at 2094 cm^{-1} in MIR; and (2) a new species (H·-dissociated species or U) which is similar with the recently discovered [Fe^{I}(DMeOPrPE)$_2$(N$_2$)]$^+$.[17] This species is supposed to have a balanced bipolar difference spectrum with a positive peak at 2056 cm^{-1} and a negative peak at 2094 cm^{-1}. While visible light photolysis produces only N$_2$-dissociated species (V) (Fig. 4a and b), photolysis including UV radiation produces both N$_2$-dissociated and H·-dissociated species (V and U) (Fig. 4c–e). Under no circumstance, photolyses without UV can produce H·-dissociated species (U) and under no circumstance, species conversion of V → U is ever observed. The downshifted ν(N≡N) stretch 2094 → 2056 cm^{-1} is consistent with the spectral difference in Fe^{I} (in **7**) *vs.* Fe^{II} (in **1**), which is observed *via* MIR and reproduced in a DFT calculation (Fig. 4g). A large Mössbauer quadrupole moment and the NIR peak positions also provide evidence for a low spin Fe^{I} complex in a UV-inclusive photolysis. On the other hand, N$_2$-dissociated species (V) can be produced *via* either visible or UV photolysis and is likely to keep a low spin Fe^{II}. For easier discussions, we define the UV/visible light divider at around 370 nm. To discuss mechanisms of the wavelength dependent photochemistry for **1** (or its isotopologues), we have the following two hypotheses as illustrated in Fig. 8a and b: (a) the N$_2$ dissociation always occurs first (producing N$_2$-dissociated species, V) followed by a thermal conversion to H· dissociation (U) because peak A is always larger in size than peak B. This hypothesis is, however, not supported by our overall experimental evidences because: (1) all bipolar MIR spectra observed for **1** must be produced *via* UV (<370 nm) irradiation – no UV, no bipolar MIR, no H·-dissociated species (U); (2) NRVS also supports 'no UV, no Fe–H cleavage'; (3) no situation is observed where the growth in B occurs in accordance with the shrink in A (meaning no conversion from A to B, or from V to U) in photolysis (Fig. 4c–e) or in recombination (Fig. 6c).

In a more possible mechanism, which is illustrated in Fig. 8b1 and b2, the N$_2$ dissociation (species V) occurs with a visible (b1) or with a UV (b2) light photolysis. It can be recombined when the photolysis product is warmed up to as low as 13 K. Fast *in situ* recombination can also exist during the photolysis with a high heat load light source. When the sample is irradiated with a UV or UV-inclusive source, the dissociation of H· along with the Fe^{II} → Fe^{I} change in **1** (U) occur in addition to the process of N$_2$ dissociation (V) as described in Fig. 8b2: the photo-detachment channels of N$_2$ *vs.* H· is then in competition with one another. Contrary to the easy recombination after the Fe–N$_2$ dissociation (species V), no recombination is observed once an H· atom has been lost (species U) – even warmed up to a temperature to as high as 120 K (Fig. 6c). N$_2$-dissociated species (V) is likely to dominate in low photon flux (low heat load) experiments, and the
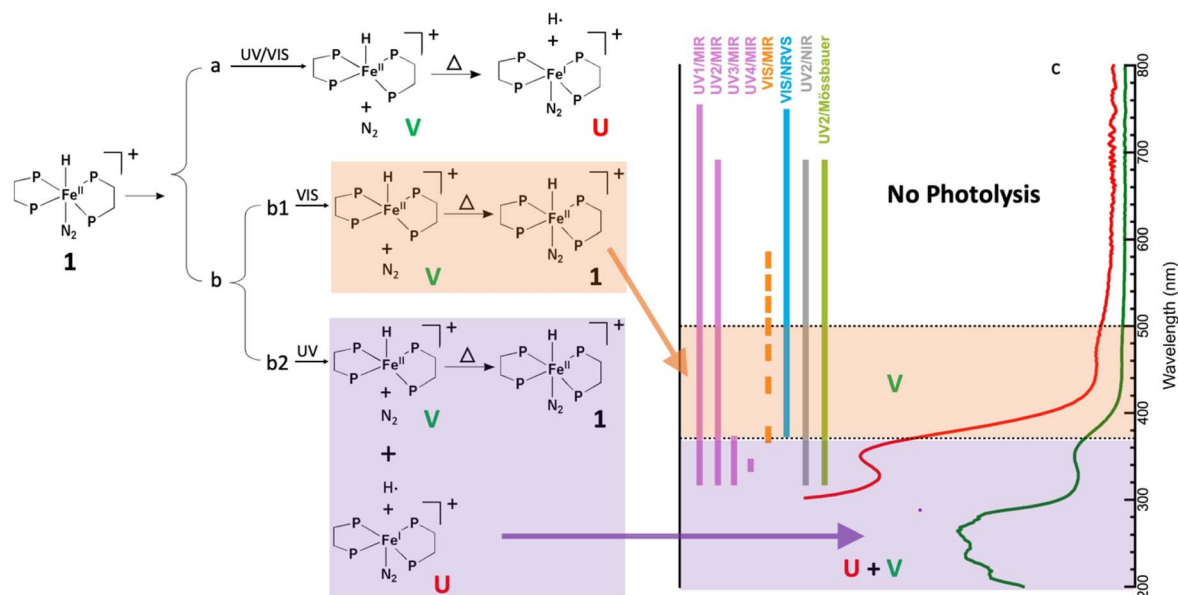
Fig. 8 (a and b) Alternate explanations for observed photochemistry of **1** while (b) is a realistic mechanism based on the overall experimental evidences obtained *via* multiple spectroscopies in this study; (c) UV-visible absorption spectrum of **1** (green curve) along with a ×5 intensity expansion (red curve). The colored bars in (c) indicate the photolysis wavelength regions in different photolysis cases, measured with MIR (UV = pink and visible light = orange yellow), NRVS (visible light, blue), NIR (UV2, grey) and Mössbauer (UV2, green). The dashed 'dividing lines' are just used as an eye guide.

process of $N_2Fe^{II}(H^-) \rightarrow N_2Fe^I + H\cdot$ (species U) starts to increase in photolyses with high heat load. This is because the produced species V can undergo *in situ* recombination back to **1** no matter it is produced in a visible light photolysis (b1) or in a UV photolysis (b2). In short, our experimental results all support the mechanism illustrated in Fig. 8b.

All our results are also consistent with the UV-visible absorption spectrum for complex **1** (Fig. 8c). In visible light photolyses, for example, Fig. 4a *vs.* b and Fig. S4a *vs.* b *vs.* c† (MIR) reveal that 372 nm irradiation leads to a much higher photolysis rate than 502 nm does. This is consistent with the much higher absorbance at 372 nm in comparison with that at 502 nm (Fig. 8c, green or red with ×5). On the other hand, all our UV photolysis wavelengths (UV1,2,3,4 as indicated with pink bars for MIR, grey bar for NIR, green bar for Mössbauer in Fig. 8c) cover the peak in the absorption spectrum around 340–360 nm (Fig. 8c) and all of the related photolyses produce H·-dissociated species (U). For example, all of them observed an Fe^I center in the photolysis product. Meanwhile, the photolysis wavelength for NRVS (the blue bar in Fig. 8c) covers about the same as the overall region of several visible light photolyses in MIR experiments (the yellow bars) and indeed no Fe–H· dissociation is observed by either (MIR or NRVS).

In short, all our experimental observations in multiple spectroscopies lead to a consistent result that visible photolysis produces only an N_2 dissociation with an Fe^{II} center while UV-inclusive photolysis leads to the competition between an N_2 dissociation with an Fe^{II} center and a H· detachment with an Fe^I center.

This work is the first wavelength dependent photolysis study with multiple spectroscopies on a reaction active N_2ase–N_2

model complex. The work also demonstrates the competition ejection between two ligands (H· and N_2). The valuable information as well as the practice of using multiple spectroscopies for the research provided us a solid first step towards the future studies on a real N_2-binding N_2ase and its photolysis products.

Experimental aspects

Please refer to the ESI† for experimental details. Here, only the most critical information is mentioned for an easier reference.

The *trans*-[Fe(DMeOPrPE)$_2$(N$_2$)H][BPh$_4$] (**1**), its isotopologues (**2–5**) and its Fe^I counterpart (**7**) were prepared by literature methods[12] at U. Oregon. Samples for photolysis studies were in THF solution while some samples for non-photolysis measurements were in powders in KBr pellets.

The photolysis was performed with either a Sutter Lambda XL (for NRVS, output = Fig. S5†) or a Sutter Lambda LS (for mid-IR, near-IR and Mössbauer, similar to Fig. S5†).

Mid IR and near-IR spectra were measured in a Bruker VERTEX 70v FT-IR spectrometer with a liquid-helium flow cryostat maintained at nominal 4 K. For most photolyses, a perpendicular setup was used where the photolysis light and IR beam were introduced from different optical pathways, which allow UV wavelengths to arrive at the samples. Additional wavelength limits can be set with different optical filters (Semrock). Another option is the "parallel" setup where the photolysis light and IR beam passed through the same IR optics, which effectively blocks the radiation <500 nm.

Far-IR absorption spectra were recorded using a Brucker IFS 66 v/S FT-IR at ALS BL1.4. Samples were measured in Nujol mull at room temperature. FT-Raman spectra were recorded in Frei's

Lab at LBNL, with a Bruker FRA-106. The samples were measured with a 50 mW laser power at 77 K. No radiation damage was observed. No photolysis was performed for far-IR or FT-Raman.

^{57}Fe NRVS spectra were measured using published procedures[13–16] at SPring-8 BL09XU or APS 3-ID. The total scattering counts from delayed nuclear fluorescence and the converted Fe K fluorescence vs. the energy difference ($E_{vib} = E - E_0$, where $E_0 = 14.4125$ keV) forms a raw NRVS spectrum. It can be further processed to a partial vibrational density of state (PVDOS) via PHOENIX,[13,14,30] starting from zero cm^{-1}. During this analysis, the real sample temperature[23] can be assessed. Photolysis of complex 5 (1-^{57}Fe/D) was measured via in situ NRVS for 12 hours. The real sample temperature[23] for the non-photolysis sample were at 50 K while that for the photolysis sample was 80 K.

Mössbauer spectra before and after photolysis on complex 4 (1-^{57}Fe) in THF were recorded on a spectrometer from SEE Co. (Edina, MN) in transmission geometry. Mössbauer spectra were recorded at 80 K (cooled with liquid nitrogen).

DFT calculations was performed analogous to those on HFeCO complex.[27,31] The computed NRVS (IR) spectra were broadened with a 7 cm^{-1} (10 cm^{-1}) Lorentzian line profile.

Data availability

All the relevant data are either in the main text or in ESI.† Various other data are also available from the authors on request.

Author contributions

WD, HW, SK, YG, LY, YY, and JZ performed photolysis experiments, measured various spectra, and/or analyzed the data (data curation/formal analysis/investigation/validation), DRT, CGB, and JLC synthesized and characterized the chemical complexes used in this study and discussed the spectroscopic results (methodology/resources/investigation), DAC provided DFT calculations (software/visualization) and SPC constructed the initial concept in, provided academic guide to and acquired financial support for the research (conceptualization/investigation/funding acquisition). WD, HW, DRT and SPC wrote and/or revised the manuscript (writing/reviewing/editing).

Conflicts of interest

There are no conflicts to declare.

Acknowledgements

References

1 R. Y. Igarashi and L. C. Seefeldt, Nitrogen Fixation: The Mechanism of the Mo-Dependent Nitrogenase, *Crit. Rev. Biochem. Mol. Biol.*, 2003, **38**, 351–384.

2 D. C. Rees, F. A. Tezcan, C. A. Haynes, M. Y. Walton, S. Andrade, O. Einsle and J. B. Howard, Structural basis of biological nitrogen fixation, *Philos. Trans. R. Soc., A*, 2005, **363**, 971–984.

3 P. C. Dos Santos, R. Y. Igarashi, H.-I. Lee, B. M. Hoffman, L. C. Seefeldt and D. R. Dean, Substrate interactions with the nitrogenase active site, *Acc. Chem. Res.*, 2005, **38**, 208–214.

4 T. Spatzal, M. Aksoyoglu, L. Zhang, S. L. A. Andrade, E. Schleicher, S. Weber, D. C. Rees and O. Einsle, Evidence for Interstitial Carbon in Nitrogenase FeMo Cofactor, *Science*, 2011, **334**, 940.

5 R. N. F. Thorneley and D. J. Lowe, in *Molybdenum Enzymes*, ed. T. G. Spiro, John Wiley and Sons, New York, 1985, pp. 221–284.

6 D. Lukoyanov, B. M. Barney, D. R. Dean, L. C. Seefeldt and B. M. Hoffman, Connecting nitrogenase intermediates with the kinetic scheme for N$_2$ reduction by a relaxation protocol and identification of the N$_2$ binding state, *Proc. Natl. Acad. Sci. U. S. A.*, 2007, **104**, 1451–1455.

7 B. M. Barney, T.-C. Yang, R. Y. Igarashi, P. C. D. Santos, M. Laryukhin, H.-I. Lee, B. M. Hoffman, D. R. Dean and L. C. Seefeldt, Intermediates Trapped during Nitrogenase Reduction of N≡N, CH$_3$-N=NH, and H$_2$N-NH$_2$, *J. Am. Chem. Soc.*, 2005, **127**, 14960–14961.

8 J. L. Crossland and D. R. Tyler, Iron-dinitrogen coordination chemistry: Dinitrogen activation and reactivity, *Coord. Chem. Rev.*, 2010, **254**, 1883–1894.

9 J. D. Gilbertson, N. K. Szymczak and D. R. Tyler, Reduction of N$_2$ to ammonia and hydrazine utilizing H$_2$ as the reductant, *J. Am. Chem. Soc.*, 2005, **127**, 10184–10185.

10 J. D. Gilbertson, N. K. Szymczak, J. L. Crossland, W. K. Miller, D. K. Lyon, B. M. Foxman, J. Davis and D. R. Tyler, Coordination chemistry of H$_2$ and N$_2$ in aqueous solution. Reactivity and Mechanistic Studies Using *trans*-Fe^{II}(P$_2$)$_2$X$_2$-Type Complexes (P$_2$= a Chelating, Water-solubilizing Phosphine), *Inorg. Chem.*, 2007, **46**, 1205–1214.

11 R. B. Yelle, J. L. Crossland, N. K. Szymczak and D. R. Tyler, Theoretical Studies of N$_2$ Reduction to Ammonia in Fe(dmpe)$_2$N$_2$, *Inorg. Chem.*, 2009, **48**, 861–871.

12 J. L. Crossland, D. M. Young, L. N. Zakharov and D. R. Tyler, Precursors to dinitrogen reduction: structures and reactivity

of *trans*-[Fe(DMeOPrPE)$_2$(η^2-H$_2$)H]$^+$ and *trans*-[Fe(DMeOPrPE)$_2$(N$_2$)H]$^+$, *Dalton Trans.*, 2009, 9253–9259, DOI: 10.1039/b911066f.

13 V. Pelmenschikov, J. A. Birrell, C. C. Pham, N. Mishra, H. Wang, C. Sommer, E. Reijerse, C. P. Richers, K. Tamasaku, Y. Yoda, T. B. Rauchfuss, W. Lubitz and S. P. Cramer, Reaction Coordinate Leading to H2 Production in [FeFe]-Hydrogenase Identified by Nuclear Resonance Vibrational Spectroscopy and Density Functional Theory, *J. Am. Chem. Soc.*, 2017, **139**, 16894–16902.

14 J. Wang, L. Li and H. Wang, Machine learning concept in de-spiking process for nuclear resonant vibrational spectra – Automation using no external parameter, *Vib. Spectrosc.*, 2022, **119**, 103352.

15 Y. Guo, H. Wang, Y. Xiao, S. Vogt, R. K. Thauer, S. Shima, P. I. Volkers, T. B. Rauchfuss, V. Pelmenschikov, D. A. Case, E. E. Alp, W. Sturhahn, Y. Yoda and S. P. Cramer, Characterization of the Fe site in iron-sulfur cluster-free hydrogenase (Hmd) and of a model compound via nuclear resonance vibrational spectroscopy (NRVS), *Inorg. Chem.*, 2008, **47**, 3969–3977.

16 H. Ogata, T. Kramer, H. Wang, D. Schilter, V. Pelmenschikov, M. van Gastel, F. Neese, T. B. Rauchfuss, L. B. Gee, A. D. Scott, Y. Yoda, Y. Tanaka, W. Lubitz and S. P. Cramer, Hydride bridge in [NiFe]-hydrogenase observed by nuclear resonance vibrational spectroscopy, *Nat. Commun.*, 2015, **6**, 7890.

17 C. G. Balesdent, J. L. Crossland, D. T. Regan, C. T. López and D. R. Tyler, Characterization of an Intermediate in the Ammonia-Forming Reaction of Fe(DMeOPrPE)2N2 with Acid (DMeOPrPE = 1,2-[bis(dimethoxypropyl)phosphino]ethane), *Inorg. Chem.*, 2013, **52**, 14178–14187.

18 L. Yan, C. H. Dapper, S. J. George, H.-X. Wang, D. Mitra, W.-B. Dong, W. E. Newton and S. P. Cramer, Photolysis of 'Hi-CO' Nitrogenase – Observation of a Plethora of Distinct CO Species via Infrared Spectroscopy, *Eur. J. Inorg. Chem.*, 2011, **2011**, 2064–2074.

19 L. Yan, V. Pelmenschikov, C. H. Dapper, A. D. Scott, W. E. Newton and S. P. Cramer, IR-Monitored Photolysis of CO-Inhibited Nitrogenase: A Major EPR-Silent Species with Coupled Terminal CO Ligands, *Chem.–Eur. J.*, 2012, **18**, 16349–16357.

20 L. B. Gee, V. Pelmenschikov, H. Wang, N. Mishra, Y.-C. Liu, Y. Yoda, K. Tamasaku, M.-H. Chiang and S. P. Cramer, Vibrational characterization of a diiron bridging hydride complex – a model for hydrogen catalysis, *Chem. Sci.*, 2020, **11**, 5487–5493.

21 O. Franke, B. E. Wiesler, N. Lehnert, G. Peters, P. Burger and F. Tuczek, The iron hydrido complex [FeH(dppe)$_2$]$^+$: Solution and Solid-State Reactivity with Dinitrogen, *Z. Anorg. Allg. Chem.*, 2006, **632**, 1247–1256.

22 M. H. Chiang, V. Pelmenschikov, L. B. Gee, Y. C. Liu, C. C. Hsieh, H. Wang, Y. Yoda, H. Matsuura, L. Li and S. P. Cramer, High-Frequency Fe-H and Fe-H(2) Modes in a trans-Fe(η(2)-H(2))(H) Complex: A Speed Record for Nuclear Resonance Vibrational Spectroscopy, *Inorg. Chem.*, 2021, **60**, 555–559.

23 H. Wang, Y. Yoda, S. Kamali, Z.-H. Zhou and S. P. Cramer, Real sample temperature: a critical issue in the experiments of nuclear resonant vibrational spectroscopy on biological samples, *J. Synchrotron Radiat.*, 2012, **19**, 257–263.

24 O. Franke, B. E. Wiesler, N. Lehnert and F. Tuczek, Vibrational properties of [FeH(N$_2$)(depe)$_2$]$^+$ and [FeCl(N$_2$)(depe)$_2$]$^+$: Dinitrogen bonding in the low activation limit, *Z. Anorg. Allg. Chem.*, 2002, **628**, 2395–2402.

25 Y. Xiao, H. Wang, S. J. George, M. C. Smith, M. W. W. Adams, J. F. E. Jenney, W. Sturhahn, E. E. Alp, J. Zhao, Y. Yoda, A. Dey, E. I. Solomon and S. P. Cramer, Normal Mode Analysis of *Pyrococcus furiosus* Rubredoxin *via* Nuclear Resonant Vibrational Spectroscopy (NRVS) and Resonance Raman Spectroscopy, *J. Am. Chem. Soc.*, 2005, **127**, 14596–14606.

26 M. C. Smith, Y. Xiao, H. Wang, S. J. George, D. Coucovanis, M. Koutmos, W. Sturhahn, E. E. Alp, J. Zhao and S. P. Cramer, Normal Mode Analysis of [FeCl$_4$]$^-$ and [Fe$_2$S$_2$Cl$_4$]$^{2-}$ *via* Vibrational Mössbauer, Resonance Raman, and FT-IR Spectroscopy, *Inorg. Chem.*, 2005, **44**, 5562–5570.

27 V. Pelmenschikov, Y. Guo, H. Wang, S. P. Cramer and D. A. Case, Fe-H/D stretching and bending modes in nuclear resonant vibrational, Raman and infrared spectroscopies: Comparisons of density functional theory and experiment, *Faraday Discuss.*, 2010, **148**, 409–420.

28 C. C. Lu, C. T. Saouma, M. W. Day and J. C. Peters, Fe(I)-Mediated Reductive Cleavage and Coupling of CO2: An Fe^{II}(*m*-O,*m*-CO)Fe^{II} Core, *J. Am. Chem. Soc.*, 2007, **129**, 2.

29 B. Fultz, in *Characterization of Materials*, ed. E. Kaufmann, John Wiley, New York, 2011.

30 M. Y. Hu, T. S. Toellner, N. Dauphas, E. E. Alp and J. Zhao, Moments in nuclear resonant inelastic x-ray scattering and their applications, *Phys. Rev. B: Condens. Matter Mater. Phys.*, 2013, **87**, 064301.

31 J. P. Perdew, K. Burke and M. Ernzerhof, Generalized Gradient Approximation Made Simple, *Phys. Rev. Lett.*, 1996, **77**, 3865–3868.